

# ISOGEOMETRIC SHAPE OPTIMIZATION FOR SCAFFOLD STRUCTURES

HELMUT HARBRECHT, MICHAEL MULTERER, AND REMO VON RICKENBACH

**ABSTRACT.** The development of materials with specific structural properties is of huge practical interest, for example, for medical applications or for the development of light weight structures in aeronautics. In this article, we combine shape optimization and homogenization for the optimal design of the microstructure in scaffolds. Given the current microstructure, we apply the isogeometric boundary element method to compute the effective tensor and to update the microstructure by using the shape gradient in order to match the desired effective tensor. Extensive numerical studies are presented to demonstrate the applicability and feasibility of the approach.

## 1. INTRODUCTION

Many engineering problems amount to boundary value problems for an unknown function, which needs to be appropriately approximated in order to infer some desired quantity of interest. If the problem under consideration exhibits different length scales, homogenization is the method of choice to avoid the expensive numerical resolution of the different scales involved. The idea of homogenization is to replace the governing mathematical equations at multiple scales by approximate governing equations which only exhibit a single scale, see [2, 4, 7, 44] for example.

Within this approach, the article at hand focuses on scaffold structures. Indeed, additive manufacturing allows to build lattices or perforated structures and hence to build structures with physical properties that vary in space. Assuming a lattice structure of the material under consideration, one may compute the effective material tensor on the microscale in order to derive an “effective” equation on the macroscale. Taking this consideration as a starting point, we address the optimal design of such scaffold structures. This task is motivated by the need of scaffold structures which realize specific properties. The efficient numerical solution of this problem has, of course, a huge impact on many practical applications. Examples range from the development of light weight structures in aeronautics to medical implants in the orthopedic and dental fields, see e.g. [27, 46] and the references therein.

---

2010 *Mathematics Subject Classification.* 49K20, 49Q10, 74Q05.

*Key words and phrases.* Scaffold structures, isogeometric boundary element method, homogenization, shape optimization.

We remark that the optimal design of scaffold structures has already been considered in many works, see [1, 8, 16, 26, 30, 31, 33, 37, 39, 40, 41, 45, 47] for some of the respective results. The methodology used there is mainly based on the forward simulation of the material properties of a given microstructure. Whereas, sensitivity analysis has been used in [3, 17] to compute the derivatives with respect to the side lengths and the orientation of rectangular cavities. In [28], the derivatives with respect to the coefficients of a B-spline parametrization of the cavity have been computed. In [35], the shape derivative has been derived in the context of a level set representation of the inclusion. Rather than pursuing one of the aforementioned approaches, we follow [9, 22] and discretize Hadamard’s shape gradient directly. Shape sensitivity analysis is a powerful tool as it gives explicit knowledge about the dependency of the functional under consideration on shape perturbations. As a consequence, we are able to perform a gradient based optimization of the scaffold structure.

Shape optimization has been proven an efficient tool for designing structures, which should be constructed with respect to certain optimal design considerations. Having the shape gradient at hand, it can be applied to optimize the structure under consideration with respect to the underlying shape functional, see [11, 34, 38, 42, 43] and the references therein for an overview on the topic of shape optimization. Note that shape optimization falls into the general setting of optimal control of partial differential equations.

For the numerical realization of our approach, we adopt the *isogeometric analysis* (IGA) framework. IGA has been introduced in [29] in order to incorporate simulation techniques into the design workflow of industrial development and thus allows to deal with domain deformations in a straightforward manner. Especially, by representing the computational geometry and deformation fields by *non-uniform rational B-splines* (NURBS), shapes can easily be deformed by directly updating the NURBS mappings which are used to represent the shape under consideration. The particular class of shape deformations considered within this work are the eigenfunctions of a prescribed covariance kernel. This way, we determine principal displacement fields that are tailored to the underlying geometry. In particular, this approach is independent of the geometry’s smoothness or genus, as we illustrate within our numerical experiments.

The cell functions, which are required for the computation of the effective tensor, are determined by means of boundary integral equations. Especially, we show that all computations can be conducted at the boundary of the cavity, including the evaluation of the shape functional and the shape gradient. This especially allows for dealing with large deformations without having to update any volume mesh. For numerical computations, we rely on the fast isogeometric boundary element method, developed in [12, 14, 15, 23], which is available as C++-library `bemvel` [12, 13]. In order to speed up computations, `bemvel` employs  $\mathcal{H}^2$ -matrices with the interpolation based fast multipole method [19, 20, 21].

This article is structured as follows. In Section 2, we briefly recall the fundamentals of homogenization theory and introduce the problem under consideration. We especially present the shape gradient which enables us to find the optimal effective tensor by means of a gradient based optimization method. The topic of Section 3 is the reformulation of the cell problem by means of boundary integral equations. This amounts to the so-called Neumann-to-Dirichlet map, where the Green's function for the periodic Laplacian is computed along the lines of [5, 6]. After having solved the Neumann-to-Dirichlet map, both, it suffices to evaluate the shape functional and the shape gradient exclusively at the boundary of the cavity. Section 4 is dedicated to the discretization of the shape optimization problem, which comprises the discretization of the shape and the discretization of the Neumann-to-Dirichlet map. Namely, we show how to define shape deformations by using the eigenfunctions of a prescribed covariance kernel. We also summarize the solution of the Neumann-to-Dirichlet map by the isogeometric boundary element method. Various numerical experiments are then performed in Section 5. We consider simple cavities like the sphere and the cube, a multiple cavity consisting of a sphere and a cube, and finally a drilled cube which is a cavity of genus 12. Finally, in Section 6, we state concluding remarks.

## 2. SHAPE OPTIMIZATION FOR SCAFFOLDS

**2.1. Homogenization.** We start by outlining the approach considered in this article. To this end, we shall restrict ourselves to the situation of the simple two-scale problem posed on a domain  $D \subset \mathbb{R}^3$ , i.e.

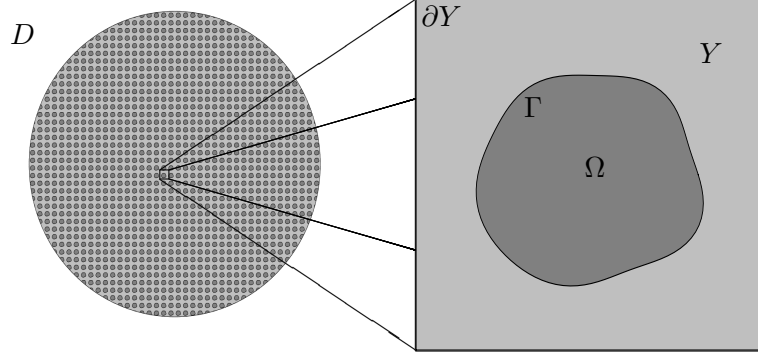
$$(1) \quad -\operatorname{div}(\mathbf{A}^\varepsilon \nabla u^\varepsilon) = f \text{ in } D, \quad u^\varepsilon = 0 \text{ on } \partial D.$$

Herein, the  $(3 \times 3)$ -matrix  $\mathbf{A}^\varepsilon$  is assumed to be oscillatory in the sense that

$$\mathbf{A}^\varepsilon(\mathbf{x}) = \mathbf{A}\left(\frac{\mathbf{x}}{\varepsilon}\right), \quad \mathbf{x} \in D.$$

Mathematical homogenization is the study of the limit of  $u^\varepsilon$  when  $\varepsilon$  tends to 0. Various approaches have been developed for this purpose. The oldest one is comprehensively presented in Bensoussan, Lions and Papanicolaou [4]. It consists of performing a formal multiscale asymptotic expansion and then, in the justification of its convergence, using the energy method due to Tartar [44]. A significant result obtained from this approach is the existence of the  $(L^2(D))$ -limit  $u_0(\mathbf{x})$  of  $u^\varepsilon(\mathbf{x})$  and, more importantly, the identification of a limiting, “effective” or “homogenized” elliptic problem in  $D$  satisfied by  $u_0$ .

We introduce the unit cell  $Y = [-1/2, 1/2]^3$  for the fast scale of problem (1) and assume that the matrix field  $\mathbf{A}(\mathbf{y})$  is  $Y$ -periodic, cf. Figure 1 for a graphical illustration. Moreover, we consider the space  $H_{\text{per}}^1(\mathbf{y})$  of  $Y$ -periodic functions with vanishing mean that belong to  $H^1(\mathbf{y})$  and the unit vector  $\mathbf{e}_i \in \mathbb{R}^3$  in the  $i$ -th direction of  $\mathbb{R}^3$ . We define the cell problems for

FIGURE 1. The domain  $D$  with unit cell  $Y$ .

$i = 1, 2, 3$  according to

$$\begin{aligned} \text{find } w_i \in H_{\text{per}}^1(\mathbf{y}) \text{ such that} \\ -\operatorname{div}(\mathbf{A}(\mathbf{y})(\mathbf{e}_i + \nabla w_i)) = 0. \end{aligned}$$

The Lax-Milgram lemma ensures the existence and uniqueness of the solutions  $w_i$  to these cell problems for  $i = 1, 2, 3$ .

The family of functions  $w_i$  then determines the *effective tensor*

$$\mathbf{A}_0 = [a_{i,j}]_{i,j=1}^3$$

in accordance with

$$a_{i,j} = \int_Y \langle \mathbf{A}(\mathbf{e}_i + \nabla w_i), \mathbf{e}_j + \nabla w_j \rangle d\mathbf{y}.$$

Based on this tensor, we may compute the *homogenized solution*  $u_0 \in H_0^1(D)$  by means of the boundary value problem

$$-\operatorname{div}(\mathbf{A}_0 \nabla u_0) = f \text{ in } D, \quad u_0 = 0 \text{ on } \partial D.$$

In particular, by setting

$$u_1(\mathbf{x}, \mathbf{y}) = \sum_{i=1}^3 \frac{\partial u_0}{\partial x_i}(\mathbf{x}) w_i(\mathbf{y}), \quad (\mathbf{x}, \mathbf{y}) \in D \times Y,$$

there holds the error estimate

$$\left\| u^\varepsilon(\mathbf{x}) - u_0(\mathbf{x}) - \varepsilon u_1\left(\mathbf{x}, \frac{\mathbf{x}}{\varepsilon}\right) \right\|_{H^1(D)} \leq c\sqrt{\varepsilon} \rightarrow 0 \text{ as } \varepsilon \rightarrow 0$$

for some constant  $c > 0$ , cf. [2, 36].

**2.2. Scaffold structures.** From now on, we shall consider a scaffold structure. To this end, we assume that the unit cell  $Y = [0, 1]^3$  is comprised of a homogeneous material which contains some cavity  $\Omega$ . More precisely, let  $\Omega$  be an open subset of  $Y$  and set  $\Gamma := \partial\Omega$ . The collection of interior boundaries, being translates of  $\varepsilon\Gamma$  of the macroscopic domain  $D^\varepsilon$ , is denoted by  $\partial D_{\text{int}}^\varepsilon$  while the remainder of the boundary  $\partial D^\varepsilon \setminus \partial D_{\text{int}}^\varepsilon$  is denoted by  $\partial D_{\text{ext}}^\varepsilon$ . The current situation is illustrated in Figure 1.

In accordance with [7], we consider the boundary value problem

$$(2) \quad \begin{aligned} -\operatorname{div}(\mathbf{A}^\varepsilon \nabla u^\varepsilon) &= f && \text{in } D^\varepsilon, \\ \langle \mathbf{A}^\varepsilon \nabla u^\varepsilon, \mathbf{n} \rangle &= 0 && \text{on } \partial D_{\text{ext}}^\varepsilon, \\ u^\varepsilon &= 0 && \text{on } \partial D_{\text{int}}^\varepsilon. \end{aligned}$$

Here, we have  $\mathbf{A}^\varepsilon = \mathbf{A}(\cdot/\varepsilon)$  in  $D^\varepsilon$  with  $\mathbf{A} = \mathbf{I}$  in  $Y \setminus \overline{\Omega}$ . Moreover, the surface  $\Gamma$  of the cavity  $\Omega$  is assumed to be oriented such that its normal vector  $\mathbf{n}$  indicates the direction going from the interior of  $\Omega$  to the exterior  $Y \setminus \overline{\Omega}$ .

To derive the homogenized problem, one introduces the cell functions  $w_i \in \mathbf{H}_{\text{per}}^1(Y \setminus \overline{\Omega})$  which are now given by the Neumann boundary value problems

$$(3) \quad \begin{aligned} \Delta w_i &= 0 && \text{in } Y \setminus \overline{\Omega}, \\ \partial_{\mathbf{n}} w_i &= -\langle \mathbf{n}, \mathbf{e}_i \rangle && \text{on } \Gamma. \end{aligned}$$

The homogenized equation becomes

$$-\operatorname{div}(\mathbf{A}_0(\Omega) \nabla u_0) = (1 - |\Omega|)f \text{ in } D, \quad u_0 = 0 \text{ on } \partial D.$$

Here, the domain  $D$  coincides with  $D^\varepsilon$  except for the holes. The effective tensor  $\mathbf{A}_0(\Omega) = [a_{i,j}(\Omega)]_{i,j=1}^3$  is now given by

$$(4) \quad a_{i,j}(\Omega) = \int_{Y \setminus \overline{\Omega}} \langle \mathbf{e}_i + \nabla w_i, \mathbf{e}_j + \nabla w_j \rangle d\mathbf{y},$$

compare [7]. Notice that  $\mathbf{A}_0(\Omega)$  is a symmetric matrix. However, it is not the identity in general, since the geometry of the cavity induces a global anisotropy.

**2.3. Shape calculus.** Considering a given tensor  $\mathbf{B} \in \mathbb{R}_{\text{sym}}^{3 \times 3}$  which describes the desired material properties, we may ask the following question: Can we find a cavity, i.e. a domain  $\Omega$ , such that the effective tensor is as close as possible to  $\mathbf{B}$ ?

In order to make the notion of closeness between matrices precise, we choose the Frobenius norm of matrices and define the shape functional  $J(\Omega)$  according to

$$(5) \quad J(\Omega) = \frac{1}{2} \|\mathbf{A}_0(\Omega) - \mathbf{B}\|_F^2 = \frac{1}{2} \sum_{i,j=1}^3 (a_{i,j}(\Omega) - b_{i,j})^2.$$

We mention, however, that it cannot be expected that every tensor can be matched by a corresponding scaffold structure.

In order to solve the corresponding minimization problem

$$J(\Omega) \rightarrow \min,$$

we shall employ shape optimization. We are hence interested in describing how the effective tensor depends on a given deformation field, which acts on the shape of the cavity  $\Omega$ . To this end, we introduce the displacement field  $\mathbf{V}: Y \rightarrow Y$  that vanishes at the boundary  $\partial Y$  of the reference cell but whose action may deform the interior boundary  $\Gamma$ . The deformation field is then a perturbation of identity  $\mathbf{T}_t = \mathbf{I} + t\mathbf{V}$ , which is a diffeomorphism for sufficiently small values  $t > 0$  and preserves  $Y$ . We denote by  $\Omega_t = \mathbf{T}_t(\Omega)$  and by  $w_i(t) \in \mathbf{H}_{\text{per}}^1(\mathbf{y})$  the solution of (3) for the cavity  $\Omega(t)$ . Then, the shape derivative of a given shape functional  $J(\Omega)$  is defined according to

$$(6) \quad J'(\Omega)[\mathbf{V}] = \lim_{t \rightarrow 0} \frac{J(\Omega_t) - J(\Omega)}{\varepsilon}.$$

The shape derivative (6) with respect to the functional (5) has been computed in [9] and is given by

$$(7) \quad J'(\Omega)[\mathbf{V}] = \sum_{i,j=1}^3 (a_{i,j}(\Omega) - b_{i,j}) a'_{i,j}(\Omega)[\mathbf{V}],$$

where the coefficients  $a'_{i,j}(\Omega)[\mathbf{V}]$  are given by

$$(8) \quad a'_{i,j}(\Omega)[\mathbf{V}] = - \int_{\Gamma} \langle \nabla_{\Gamma} \phi_i, \nabla_{\Gamma} \phi_j \rangle \langle \mathbf{V}, \mathbf{n} \rangle d\sigma \quad \text{with } \phi_i = x_i + w_i.$$

### 3. BOUNDARY INTEGRAL EQUATION FOR THE CELL PROBLEM

**3.1. Green's function.** In order to numerically solve the cell problem (3), we shall recast it as a boundary integral equation. To that end, we have first to determine the  $Y$ -periodic kernel function  $k_{\text{per}}(\mathbf{z})$  which satisfies  $-\Delta k_{\text{per}}(\mathbf{z}) = \delta_{\mathbf{0}}(\mathbf{z})$ . We follow [5, 6] and make the ansatz

$$k_{\text{per}}(\mathbf{z}) = \frac{1}{4\pi} \sum_{\mathbf{m} \in \{-1,0,1\}^3} \frac{1}{\|\mathbf{z} - \mathbf{m}\|} + \frac{\|\mathbf{z}\|^2}{6} + k_{\text{corr}}(\mathbf{z}),$$

where the correction  $k_{\text{corr}}(\mathbf{z})$  is given by

$$(9) \quad k_{\text{corr}}(\mathbf{z}) = \sum_{n=0}^{\infty} \sum_{\ell=-n}^n \alpha_{n,\ell} R_{\ell}^n(\mathbf{z}).$$

Here,  $\{R_{\ell}^n\}$  denote the (regular) solid harmonics and the coefficients  $\{\alpha_{n,\ell}\}$  are chosen such that  $k_{\text{per}}(\mathbf{z})$  is  $Y$ -periodic. In practice, we truncate the expansion after  $N$  terms and compute the coefficients  $\alpha_{n,\ell}$  by minimizing the deviation of  $k_{\text{per}}$  from a  $Y$ -periodic function. The necessary truncation rank to achieve machine precision is rather small. For example, we use  $N = 12$  to obtain an accuracy of about  $5 \cdot 10^{-8}$ . The coefficients  $\alpha_{n,\ell}$  can of

course be computed in an offline phase and may then be tabulated for later use.

**3.2. Neumann-to-Dirichlet map.** Having the periodic Green's function at hand, we define the corresponding single layer operator  $\mathcal{V}$  in accordance with

$$(10) \quad \mathcal{V}: H^{-1/2}(\Gamma) \rightarrow H^{1/2}(\Gamma), \quad (\mathcal{V}w)(\mathbf{x}) = \int_{\Gamma} k_{\text{per}}(\mathbf{x} - \mathbf{y})w(\mathbf{y})d\mathbf{o}_{\mathbf{y}}$$

and the double layer operator  $\mathcal{K}$  in accordance with

$$(11) \quad \mathcal{K}: H^{1/2}(\Gamma) \rightarrow H^{1/2}(\Gamma), \quad (\mathcal{K}w)(\mathbf{x}) = \int_{\Gamma} \frac{\partial k_{\text{per}}}{\partial \mathbf{n}_{\mathbf{y}}}(\mathbf{x} - \mathbf{y})w(\mathbf{y})d\mathbf{o}_{\mathbf{y}}.$$

Given the Neumann data  $-\langle \mathbf{n}, \mathbf{e}_i \rangle$  of the cell function  $w_i \in H_{\text{per}}^1(Y \setminus \bar{\Omega})$  at the boundary  $\Gamma$ , the respective Dirichlet data are given by the solution of the boundary integral equation

$$(12) \quad \left(\frac{1}{2} - \mathcal{K}\right)w_i = \mathcal{V}\langle \mathbf{n}, \mathbf{e}_i \rangle.$$

This (exterior) Neumann-to-Dirichlet map is known to be uniquely solvable.

**3.3. Evaluating the shape functional and its gradient.** In this section, we present the formulas to compute the effective tensor  $\mathbf{A}_0(\Omega) = [a_{i,j}(\Omega)]_{i,j=1}^3$  given by (4) and its shape derivative (8) from the Dirichlet and Neumann data of the the cell function.

**Lemma 3.1.** *The effective tensor  $\mathbf{A}_0(\Omega) = [a_{i,j}(\Omega)]_{i,j=1}^3$  from (4) satisfies the identity*

$$a_{i,j}(\Omega) = \delta_{i,j}|Y \setminus \bar{\Omega}| - \int_{\Gamma} w_i \langle \mathbf{e}_j, \mathbf{n} \rangle d\mathbf{o}.$$

*Proof.* We will discuss the four terms of the effective tensor

$$a_{i,j}(\Omega) = \int_{Y \setminus \bar{\Omega}} \{ \langle \mathbf{e}_i, \mathbf{e}_j \rangle + \langle \nabla w_i, \mathbf{e}_j \rangle + \langle \mathbf{e}_i, \nabla w_j \rangle + \langle \nabla w_i, \nabla w_j \rangle \} d\mathbf{y}.$$

separately. For the first term, it holds

$$\int_{Y \setminus \bar{\Omega}} \langle \mathbf{e}_i, \mathbf{e}_j \rangle d\mathbf{y} = \delta_{i,j}|Y \setminus \bar{\Omega}|.$$

Then, integration by parts gives

$$\int_{Y \setminus \bar{\Omega}} \langle \nabla w_i, \nabla w_j \rangle d\mathbf{y} = - \int_{\Gamma} \frac{\partial w_i}{\partial \mathbf{n}} w_j d\mathbf{o} = \int_{\Gamma} \langle \mathbf{n}, \mathbf{e}_i \rangle w_j d\mathbf{o},$$

where we used the  $Y$ -periodicity of  $w_i$  and  $w_j$ . Likewise, observing that  $\text{div}(\mathbf{e}_j) = 0$ , we find for the mixed terms by integration by parts that

$$\int_{Y \setminus \bar{\Omega}} \langle \nabla w_i, \mathbf{e}_j \rangle d\mathbf{y} = - \int_{\Gamma} w_i \langle \mathbf{e}_j, \mathbf{n} \rangle d\mathbf{o}.$$

The assertion is now obtained by adding up the different terms.  $\square$

For the shape derivative of the effective tensor, we find the following expression.

**Lemma 3.2.** *The shape derivative of the effective tensor  $\mathbf{A}_0(\Omega)$  from (4) is given by*

$$a'_{i,j}(\Omega)[\mathbf{V}] = \int_{\Gamma} \{ \langle \mathbf{e}_i + \nabla_{\Gamma} w_i, \mathbf{e}_j + \nabla_{\Gamma} w_j \rangle - \langle \mathbf{e}_i, \mathbf{n} \rangle \langle \mathbf{e}_j, \mathbf{n} \rangle \} \langle \mathbf{V}, \mathbf{n} \rangle d\mathbf{o}.$$

*Proof.* Since  $\phi_i = x_i + w_i$ , we find

$$a'_{i,j}(\Omega)[\mathbf{V}] = \int_{\Gamma} \langle \mathbf{e}_i - \langle \mathbf{e}_i, \mathbf{n} \rangle \mathbf{n} + \nabla_{\Gamma} w_i, \mathbf{e}_j - \langle \mathbf{e}_j, \mathbf{n} \rangle \mathbf{n} + \nabla_{\Gamma} w_j \rangle \langle \mathbf{V}, \mathbf{n} \rangle d\mathbf{o}.$$

First, we note that the normal  $\mathbf{n}$  and the tangential gradient  $\nabla_{\Gamma} w_i$  are perpendicular to each other, i.e.  $\langle \nabla_{\Gamma} w_i, \mathbf{n} \rangle = \langle \mathbf{n}, \nabla_{\Gamma} w_j \rangle = 0$ . Moreover, we conclude

$$\langle \mathbf{e}_i - \langle \mathbf{e}_i, \mathbf{n} \rangle \mathbf{n}, \mathbf{e}_j - \langle \mathbf{e}_j, \mathbf{n} \rangle \mathbf{n} \rangle = \langle \mathbf{e}_i, \mathbf{e}_j \rangle - \langle \mathbf{e}_i, \mathbf{n} \rangle \langle \mathbf{e}_j, \mathbf{n} \rangle.$$

Therefore, we get the desired result.  $\square$

## 4. DISCRETIZATION

**4.1. Parametric representation of the reference shape.** Our goal is to compute the deformation of a given reference boundary  $\Gamma_{\text{ref}}$  such that the effective tensor  $\mathbf{A}_0(\Omega)$  corresponds to the desired one  $\mathbf{B}$ . In the following, we will assume the usual isogeometric setting for the reference boundary  $\Gamma_{\text{ref}}$ . To this end, let the unit square be denoted by  $\square := [0, 1]^2$  and assume that the reference boundary  $\Gamma_{\text{ref}}$  is represented by a regular and non-overlapping decomposition into smooth, quadrangular *patches*

$$\Gamma_{\text{ref}} = \bigcup_{i=1}^M \Gamma_{\text{ref}}^{(i)}.$$

Here, regular and non-overlapping means that the intersection  $\Gamma_{\text{ref}}^{(i)} \cap \Gamma_{\text{ref}}^{(i')}$  of two patches consists at most of a common vertex or a common edge for  $i \neq i'$ .

Following the paradigm of isogeometric analysis, each patch  $\Gamma_{\text{ref}}^{(i)}$  is represented by an invertible spline or NURBS mapping

$$(13) \quad \mathbf{s}_i: \square \rightarrow \Gamma_{\text{ref}}^{(i)} \quad \text{with} \quad \Gamma_{\text{ref}}^{(i)} = \mathbf{s}_i(\square) \quad \text{for } i = 1, 2, \dots, M.$$

We especially follow the common convention that parametrizations with a common edge coincide except for orientation.

A mesh of level  $j$  on  $\Gamma$  is finally induced by dyadic subdivisions of depth  $j$  of the unit square into  $4^j$  squares. We denote these squares by

$$\square_{k,k'}^{(j)} := [2^{-j}k, 2^{-j}(k+1)] \times [2^{-j}k', 2^{-j}(k'+1)].$$

This generates  $4^j M$  *elements* (or elementary domains), compare Figure 2.

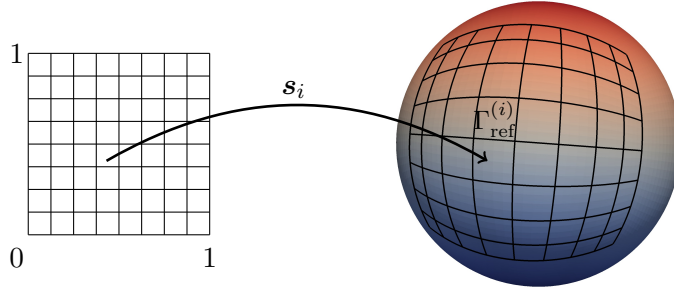


FIGURE 2. Surface representation and mesh generation.

**4.2. Shape discretization.** By assumption, the NURBS patches under consideration are smooth. As a consequence, we may reinterpolate them by using piecewise polynomials in order to speed up computations in the optimization and update procedures. More precisely, given the vertices of the subdivided unit square

$$\boldsymbol{\xi}_{\ell,\ell'} := 2^{-j} \begin{bmatrix} \ell \\ \ell' \end{bmatrix}, \quad \ell, \ell' = 0, 1, \dots, 2^j,$$

we represent the element

$$\Gamma_{i,j,k,k'} := \mathbf{s}_i(\square_{k,k'}^{(j)})$$

by piecewise interpolating the parametrization  $\mathbf{s}_i$  by tensor product polynomials of degree  $\mathbf{p} = (p_1, p_2)$ . To that end, we introduce the vertices

$$\mathbf{s}_i(\boldsymbol{\xi}_{\ell,\ell'}) \quad \text{for } \ell = m, m+1, m+p_1, \ell' = m', m'+1, \dots, m'+p_2,$$

where  $m := \min\{k, 2^j - p_1\}$ ,  $m' := \min\{k', 2^j - p_2\}$ , and the Lagrange polynomials  $L_0^{(1)}(x), L_1^{(1)}(x), \dots, L_{p_1}^{(1)}(x)$  with respect to the abscissae  $x_\ell := 2^{-j}(m+\ell)$  and  $L_0^{(2)}(y), L_1^{(2)}(y), \dots, L_{p_2}^{(2)}(y)$  with respect to  $y_{\ell'} := 2^{-j}(m'+\ell')$ . Now, we approximate

$$(14) \quad \mathbf{s}_i|_{\square_{k,k'}^{(j)}} \approx \left( \sum_{\ell=m}^{m+p_1} \sum_{\ell'=m'}^{m'+p_2} \mathbf{s}_i(\boldsymbol{\xi}_{\ell,\ell'}) L_\ell^{(1)} \otimes L_{\ell'}^{(2)} \right) \Big|_{\square_{k,k'}^{(j)}}.$$

Here, the polynomial degree  $\mathbf{p}$  is always chosen such that the overall consistency error is met.

We remark that the polynomial approximation (14) particularly allows for the rapid evaluation of geometric quantities, such as the surface measure and the normal vector by means of the complete Horner scheme if the Newton basis is used for representing the polynomials.

For the representation of shape variations, we adopt an approach that is well established in the context of random domain variations: we represent these variations by means of the Karhunen-Loève expansion, see [18, 32], of

a parametric deformation field with design parameters  $\{y_k\}_k$ , that is

$$(15) \quad \boldsymbol{\chi}(\mathbf{x}, \mathbf{y}) = \mathbf{x} + \sum_{k=1}^{\infty} \sqrt{\lambda_k} \mathbf{V}_k(\mathbf{x}) y_k, \quad \mathbf{x} \in \Gamma_{\text{ref}}.$$

Herein,  $\{\lambda_k, \mathbf{V}_k\}_k$  are the eigenpairs of the Hilbert-Schmidt operator associated to some matrix valued covariance function

$$(16) \quad \text{Cov}[\boldsymbol{\chi}]: \Gamma_{\text{ref}} \times \Gamma_{\text{ref}} \rightarrow \mathbb{R}^{d \times d}.$$

To represent the covariance structure of the interpolation points

$$\Xi := \{\mathbf{s}_i(\boldsymbol{\xi}_{\ell, \ell'}) : i = 1, 2, \dots, M, \ell, \ell' = 0, 1, \dots, 2^j\},$$

it is sufficient to consider the matrix

$$\mathbf{C} := [\text{Cov}[\boldsymbol{\chi}](\boldsymbol{\xi}, \boldsymbol{\xi}')], \quad \boldsymbol{\xi}, \boldsymbol{\xi}' \in \Xi.$$

Since  $\mathbf{C} \in \mathbb{R}^{3M(2^j+1)^2 \times 3M(2^j+1)^2}$ , the solution of the corresponding eigenvalue problem can easily become prohibitive. Therefore, we shall rely on an approach based on the pivoted Cholesky decomposition, compare [24, 25]. Assuming that  $\mathbf{C} \approx \mathbf{L}\mathbf{L}^\top$  with  $\text{rank } \mathbf{L} = p \ll 3M(2^j+1)^2$ , we can replace the eigenvalue problem  $\mathbf{L}\mathbf{L}^\top \mathbf{v} = \lambda \mathbf{v}$  by the much smaller one  $\mathbf{L}^\top \mathbf{L} \tilde{\mathbf{v}} = \lambda \tilde{\mathbf{v}}$ . Having computed an eigenpair  $(\lambda, \tilde{\mathbf{v}}_i)$  of the latter, then  $(\lambda_k, \mathbf{v}_k)$  with  $\mathbf{v}_k := \mathbf{L} \tilde{\mathbf{v}}_k$  is an eigenpair of the original eigenvalue problem. Especially, there holds  $\mathbf{v}_k^\top \mathbf{v}_k = \lambda_k$ .

As we consider a shape optimization problem, we will drop the weighting induced by the eigenvalues  $\{\lambda_k\}_k$  and consider only the eigenvectors  $\{\mathbf{v}_k\}_k$  as principal directions for the domain deformation. Then, by applying the interpolation procedure described earlier, we arrive at the parametric surface representation

$$(17) \quad \Gamma(\mathbf{y}) := \boldsymbol{\chi}(\Gamma_{\text{ref}}, \mathbf{y}) = \Gamma_{\text{ref}} + \sum_{k=1}^p \mathbf{V}_k(\mathbf{x}) y_k, \quad \mathbf{y} \in \mathbb{R}^p,$$

where the displacement fields  $\mathbf{V}_k$  are obtained by polynomial interpolation of the discrete points encoded by  $\mathbf{v}_k$ .

**4.3. Boundary element method.** We discretize the Neumann-to-Dirichlet map by means of an isogeometric Galerkin discretization. To this end, let  $\{\varphi_{j,k}\}$  denote a suitable B-spline basis of order  $d$  on the mesh of level  $j$  and define the system matrices

$$\mathbf{S}_j = \left[ \int_{\Gamma} (\mathcal{V}\varphi_{j,k'}) (\mathbf{x}) \varphi_{j,k} (\mathbf{x}) d\sigma \right]_{k,k'}, \quad \mathbf{K}_j = \left[ \int_{\Gamma} (\mathcal{K}\varphi_{j,k'}) (\mathbf{x}) \varphi_{j,k} (\mathbf{x}) d\sigma \right]_{k,k'}.$$

They correspond to the single layer operator (10) and double layer operator (11), respectively. Moreover, we require the mass matrix and the right-hand sides

$$\mathbf{M}_j = \left[ \int_{\Gamma} \varphi_k (\mathbf{x}) \varphi_{j,k'} (\mathbf{x}) d\sigma \right]_{k,k'}, \quad \mathbf{b}_{i,j} = \left[ \int_{\Gamma} \langle \mathbf{e}_i (\mathbf{x}), \mathbf{n}(\mathbf{x}) \rangle \varphi_{j,k} (\mathbf{x}) d\sigma \right]_k,$$

where  $i = 1, 2, 3$ . Then, the discrete version of the Neumann-to-Dirichlet map (12) for the computation of the cell functions  $w_i \approx \sum_k [\mathbf{w}_{i,j}]_k \varphi_{j,k}$  is given by the linear system of equations

$$(18) \quad \left( \frac{1}{2} \mathbf{M}_j + \mathbf{K}_j \right) \mathbf{w}_{i,j} = \mathbf{S}_j \mathbf{M}_j^{-1} \mathbf{b}_{i,j}.$$

In practice, we use globally continuous B-spline functions for the Dirichlet data and patchwise continuous B-spline functions for the Neumann data, as the Neumann data cannot be expected to be continuous across patch boundaries if the geometry under consideration exhibits corners and edges.

The implementation of the discretized Neumann-to-Dirichlet map (18) is done with the help of the C++-library `bemvel`, where the order of the B-splines can be chosen arbitrarily. We refer the reader to [12, 13] for the details concerning `bemvel`.

Having the Neumann and Dirichlet data of the cell functions at hand, we are able to compute the shape functional (5) and the shape gradient (7) in accordance with Lemmata 3.1 and 3.2.

## 5. NUMERICAL RESULTS

In this section, we present extensive numerical results to demonstrate the feasibility of our approach. The following setup is chosen: The covariance kernel (16) for generating the displacement fields  $\mathbf{V}_k$  in (15) is chosen diagonally with diagonal entries given by the Matèrn kernel with smoothness index  $\nu = 9/2$ , that is

$$(19) \quad k_{9/2}(r) = \left( 1 + \frac{3r}{\ell} + \frac{27r^2}{7\ell^2} + \frac{18r^3}{7\ell^3} + \frac{27r^4}{35\ell^3} \right) \exp \left( -\frac{3r}{\ell} \right),$$

where the radius is given by  $r = \|\mathbf{x} - \mathbf{y}\|_2$  and  $\ell$  denotes the correlation length. Notice that the Matèrn kernels  $k_\nu$  are the reproducing kernels of the Sobolev spaces  $H^{\nu+3/2}(\mathbb{R}^3)$ . The correlation length is always set to  $\ell = 1$ , unless otherwise stated.

In the subsequent examples, we consider a sphere, a cube and a drilled cube as initial shapes. The shape discretization is based on  $p = 16$  displacement vectors except for the drilled cube, see Section 5.4. The iterative optimization of the initial shape  $\Omega$  is performed by using the gradient descent method with quadratic line search, where convergence was always obtained within 25 steps. The boundary element method for solving the state equation employs quadratic B-spline functions on refinement level  $j = 4$ , which amounts to about 1700 boundary elements on the sphere and also on the cube. In case of the drilled cube, we use refinement level  $j = 3$ , which yields 4000 boundary elements.

As the shapes are three-dimensional, we display them with respect to different directions. The first image is always oriented such that we are

looking into  $x$ -direction, the second one such that we are looking into  $y$ -direction and the third one such that we are looking into  $z$ -direction, see Figure 3 for the orientation axes.

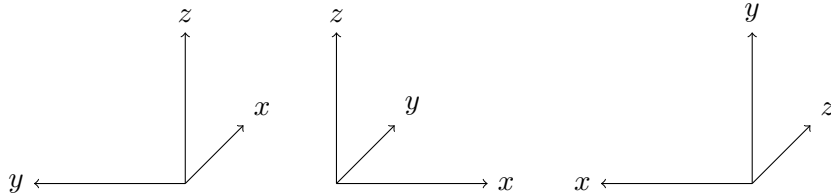


FIGURE 3. The coordinate axes for the plots of the resulting geometries.

The shape functional assumes very small values in each of the numerical examples, which indicates that the solution is not unique and depends on the particular choice of the displacement vectors. Indeed, it has already been observed in [9] that the solution of the shape optimization problem under consideration depends on the choice of the initial shape. This is also observed in our numerical experiments, as we present different optimal shapes for the same desired effective tensors.

**5.1. Sphere.** We start with the canonical example of the sphere. To this end, let us denote an open ball with radius  $r$ , centred around the point  $\mathbf{x} \in \mathbb{R}^3$ , by  $B_r(\mathbf{x}) = \{\mathbf{y} \in \mathbb{R}^3 : \|\mathbf{y} - \mathbf{x}\|_2 < r\}$ . Then, in the following examples, we use the ball  $B_{0.3}(\mathbf{0})$  as the initial shape and the optimization is stopped if  $J(\Omega) < 10^{-5}$ . For the sphere as an initial guess, this criterion was satisfied in the subsequent experiments after 3, 6, 17, and 25 iterations, respectively.

In our first test, we used

$$\mathbf{B}_1 = 0.9\mathbf{I} \quad \text{and} \quad \mathbf{B}_2 = 0.6\mathbf{I}$$

as desired effective tensor  $\mathbf{B}$  in (5). This choice yields just a scaling of the radius of the ball, compare Figure 4 for  $\mathbf{B}_1$  and Figure 5 for  $\mathbf{B}_2$ .

To obtain an ellipsoid, we prescribe an anisotropic effective tensor  $\mathbf{B}$  in (5). Let us therefore define the matrix

$$\mathbf{B}_3 = \begin{bmatrix} 0.9 & & \\ & 0.88 & \\ & & 0.86 \end{bmatrix}.$$

Using  $\mathbf{B}_3$  as the desired effective tensor, the shape of the cavity changes significantly, as can be seen in Figure 6.

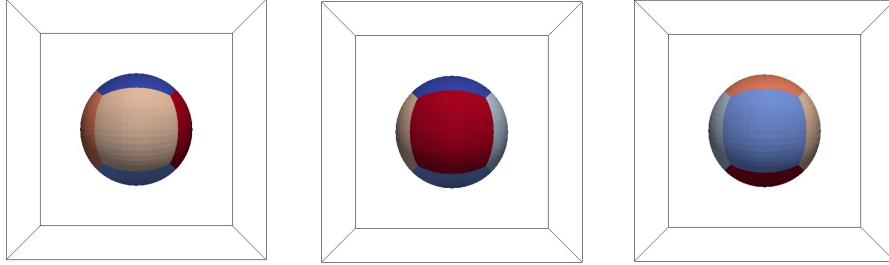


FIGURE 4. Desired tensor  $\mathbf{B}_1$ : Starting from the initial guess  $B_{0.3}(\mathbf{0})$ , one obtains a ball of approximate radius 0.25.

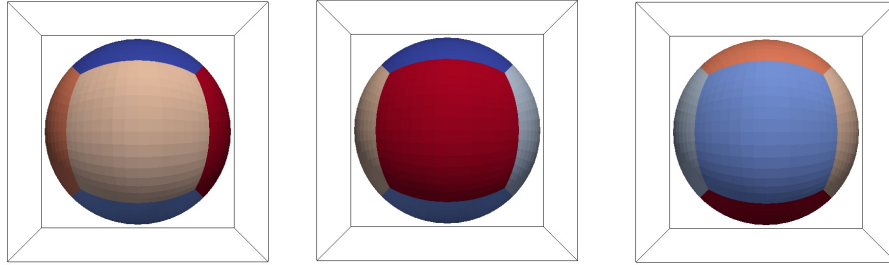


FIGURE 5. Desired tensor  $\mathbf{B}_2$ : Starting with the initial guess  $B_{0.3}(\mathbf{0})$ , one obtains a ball of approximate radius 0.42.

In order to account for shapes which are not oriented along the coordinate axes, we define the orthogonal transformation

$$(20) \quad \mathbf{T} = \begin{bmatrix} \frac{1}{\sqrt{3}} & 0 & \frac{2}{\sqrt{6}} \\ \frac{1}{\sqrt{3}} & -\frac{1}{\sqrt{2}} & -\frac{1}{\sqrt{6}} \\ \frac{1}{\sqrt{3}} & \frac{1}{\sqrt{2}} & -\frac{1}{\sqrt{6}} \end{bmatrix}$$

and choose the desired effective tensor

$$\mathbf{B}_4 = \mathbf{T}\mathbf{B}_3\mathbf{T}^\top,$$

i.e. a rotated version of the matrix  $\mathbf{B}_3$ . As can be seen in Figure 7, the perforation orients differently. Indeed, it is now aligned to the rotated coordinate system induced by the transformation  $\mathbf{T}$ .

**5.2. Cube.** In the next examples, we consider the cube  $\mathcal{C} = [-0.15, 0.15]^3$  and its rotated version  $\mathbf{T}\mathcal{C}$ , respectively, as initial guesses. We want to examine what happens if we optimize its shape with respect to a given desired effective tensor. In all examples, convergence to the final value was achieved between 13 and 16 iterations.

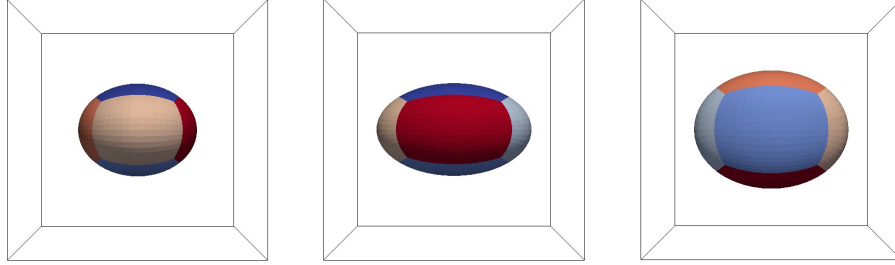


FIGURE 6. Resulting shape in case of the initial guess is  $B_{0,3}(\mathbf{0})$  and the desired tensor  $\mathbf{B}_3$ .

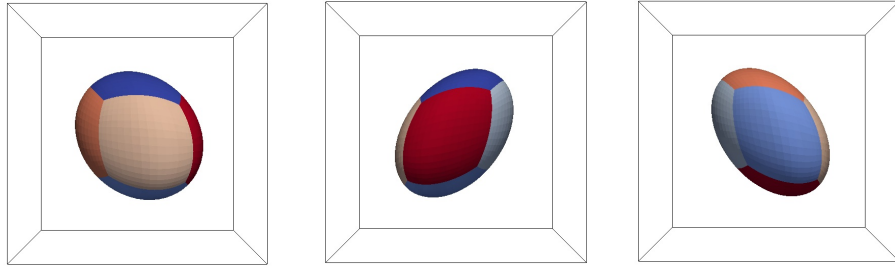


FIGURE 7. Resulting shape in case of the initial guess is  $B_{0,3}(\mathbf{0})$  and the desired tensor  $\mathbf{B}_4$ .

If the effective tensor is diagonal relative to the axes of the initial cube, then we observe that  $\Omega$  takes the shape of a cuboid, aligned with these axes. If not, then  $\Omega$  takes approximately the shape of a parallelepiped. This behaviour can clearly be observed in Figures 8–11. Therein, the first situation (initial guess and desired effective tensor aligned) appears in Figures 8 and 11, while the second situation (initial guess and desired effective tensor not aligned) appears in Figures 9 and 10.

**5.3. Sphere and cube.** Another important configuration we investigate is the situation of two initial shapes which are not connected but placed at different locations in the micro cell  $Y$ . To study this case, we define the geometry

$$\mathcal{D} = B_{0,15} \left( - [0.25, 0.25, 0.25]^\top \right) \cup [0.175, 0.325]^3.$$

The desired material tensor under consideration is the diagonal matrix

$$\mathbf{B}_5 = \begin{bmatrix} 1 & & \\ & 0.995 & \\ & & 0.99 \end{bmatrix}.$$

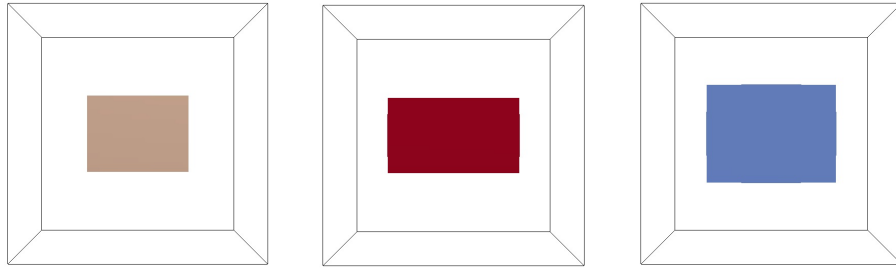


FIGURE 8. Resulting shape in case of the initial guess is  $\mathcal{C}$  and the desired tensor  $\mathbf{B}_3$ .

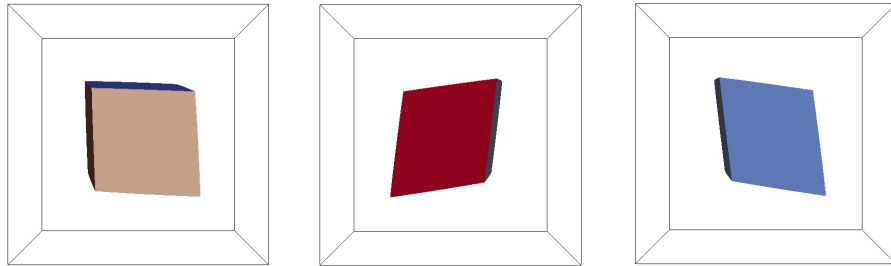


FIGURE 9. Resulting shape in case of the initial guess is  $\mathcal{C}$  and the desired tensor  $\mathbf{B}_4$ .

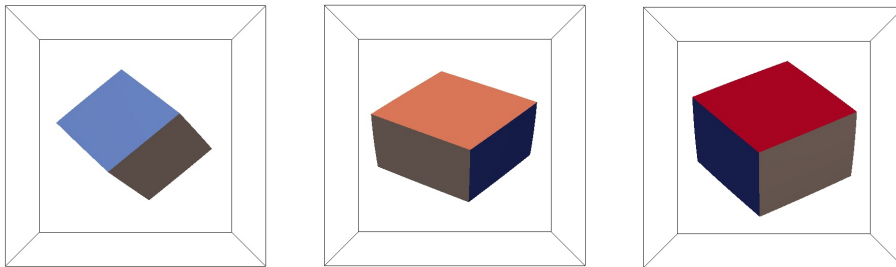


FIGURE 10. Resulting shape in case of the initial guess is  $\mathcal{TC}$  and the desired tensor  $\mathbf{B}_3$ .

As can be seen from Figure 12, using  $\mathcal{D}$  as initial guess, the geometries do not just deform as before, but rather affect each other. Especially the cube is stretched towards the (deformed) sphere.

Instead of considering different desired tensors as in the examples before, we follow a different approach here. Recall that the construction of the displacement fields depends on the Matérn kernel (19), where  $\ell > 0$  denotes

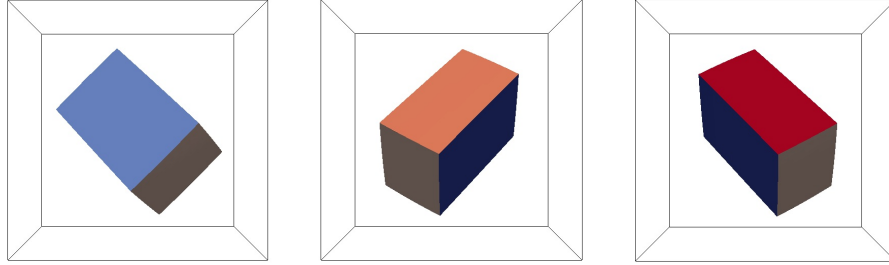


FIGURE 11. Resulting shape in case of the initial guess is  $TC$  and the desired tensor  $B_4$ .

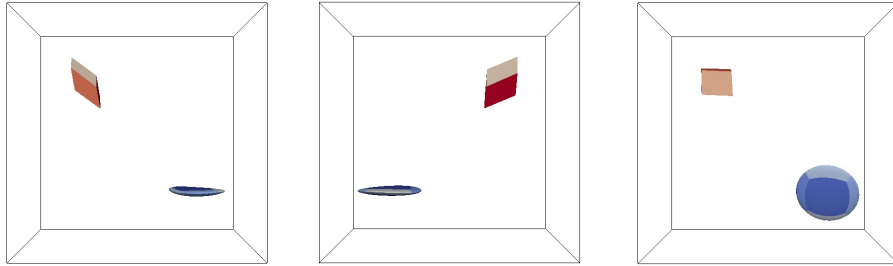


FIGURE 12. Desired tensor  $B_5$ , initial guess  $\mathcal{D}$ ,  $\ell = 1$ . Convergence is achieved after 12 iterations, computed on the fourth refinement level.

the correlation length. If  $\ell$  is chosen small, then the two shapes act more like two different geometries, compare Figure 13. However,  $p = 16$  are too few displacement fields to decrease the value of the objective functional within a reasonable amount of iterations. Hence, we rather work with  $p = 50$  displacement fields here, resulting in a rapid convergence. Note that the number of iterations to reduce the value of the shape functional below  $10^{-5}$  has been 12 when  $\ell = 1$  and 8 when  $\ell = 1/4$ .

**5.4. Drilled cube.** In our final example, we consider a more complex geometry as initial guess, namely a cube  $[-0.3, 0.3]^3$ , where three holes of diameter 0.15 have been drilled into, compare Figure 14. Notice that the parametrization of the cube is represented by 48 patches.

We choose the desired effective tensor

$$B_6 = \begin{bmatrix} 0.82 & & \\ & 0.78 & \\ & & 0.74 \end{bmatrix}$$

and employ  $p = 200$  displacement fields. We require 8 gradient descent steps to reduce the value of the shape functional below  $10^{-5}$ . The resulting shape

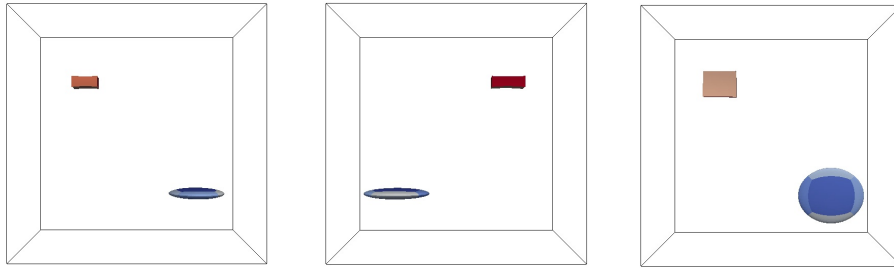


FIGURE 13. Desired tensor  $\mathbf{B}_3$ , initial guess  $\mathcal{D}$ ,  $\ell = 1/4$ . Convergence is achieved after 8 iterations, computed on the fourth refinement level.

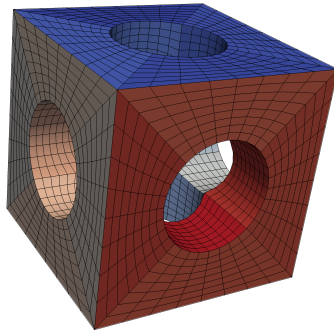


FIGURE 14. The parametrization of the drilled cube by 48 patches with mesh on refinement level 2.

is illustrated in Figure 15. It can be observed that, instead of changing the size of the cube, the size of the holes is changed in order to account for the anisotropic effective tensor.

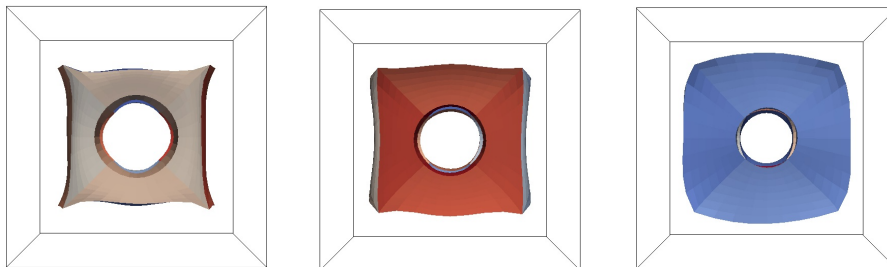


FIGURE 15. Drilled cube as initial guess for the desired tensor  $\mathbf{B}_6$ . The number of deformation vectors is  $p = 200$  and convergence is achieved after 8 gradient steps.

If we reduce the number of shape deformation vectors to  $p = 50$ , then the result is different. The latter situation is depicted in Figure 16. Here, we observe that the drilled cube (including the drill holes) is basically just rescaled to a cuboid which reflects the desired anisotropic effective tensor.

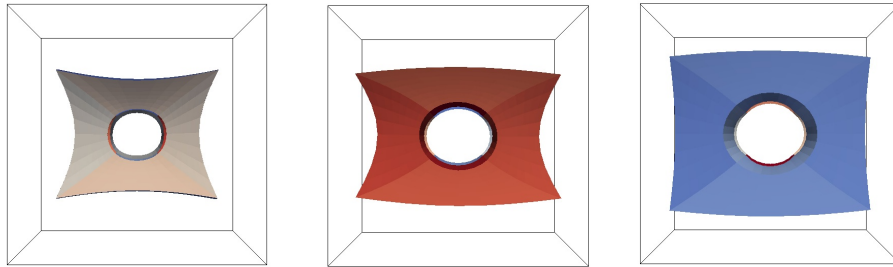


FIGURE 16. Drilled cube as initial guess for the desired tensor  $\mathbf{B}_6$ . The number of deformation vectors is  $p = 50$  and convergence is achieved after 12 gradient steps.

## 6. CONCLUSION

In this article, we have presented an isogeometric approach to the shape optimization of scaffold structures. By defining the shape deformations with the help of a covariance kernel, we are able to optimize also non-smooth shapes with edges and corners as well as disconnected shapes and shapes of genus larger than 0 without any additional effort. This implies a huge progress compared to previous approaches in shape optimization. In combination with an isogeometric boundary element method, we arrive hence at a powerful new methodology for the numerical solution of shape optimization problems.

## REFERENCES

- [1] T. Adachi, Y. Osako, M. Tanakaa, M. Hojo, and S.J. Hollister. Framework for optimal design of porous scaffold microstructure by computational simulation of bone regeneration. *Biomaterials* **27** (2006) 3964–3972.
- [2] G. Allaire. Homogenization and two-scale convergence. *SIAM J. Math. Anal.* **23** (1992) 1482–1518.
- [3] G. Allaire, P. Geoffroy-Donders, and O. Pantz. Topology optimization of modulated and oriented periodic microstructures by the homogenization method. *Comput. Math. Appl.* **78**(7) (2019) 2197–2229.
- [4] A. Bensoussan, J.-L. Lions, and G. Papanicolaou. *Asymptotic Analysis for Periodic Structures*. North-Holland, Amsterdam, 1978.
- [5] A. Barnett and L. Greengard. A new integral representation for quasi-periodic fields and its application to two-dimensional band structure calculations. *J. Comput. Phys.* **229** (2010) 6898–6914.

- [6] P. Cazeaux and O. Zahm, A fast boundary element method for the solution of periodic many-inclusion problems via hierarchical matrix techniques. *ESAIM: Proc. Surveys* **48** (2015) 156–168.
- [7] D. Cioranescu and J. Saint Jean Paulin. *Homogenization of Reticulated Structures*. Springer, New York, 1999.
- [8] L. Colabella, A.P. Cisilino, V. Fachinotti, and P. Kowalczyk. Multiscale design of elastic solids with biomimetic cancellous bone cellular microstructures. *Struct. Multidiscip. Optim.* **60** (2019) 639–661.
- [9] M. Dambrine and H. Harbrecht. Shape optimization for composite materials and scaffolds. *Multiscale Model. Sim.* **18**(2) (2020) 1136–1152.
- [10] M. Dambrine, J. Sokolowski, and A. Zochowski. On stability analysis in shape optimization: critical shapes for Neumann problem. *Control Cybernet.* **32** (2003) 503–528.
- [11] M. Delfour and J.-P. Zolesio. *Shapes and Geometries*. SIAM, Philadelphia, 2001.
- [12] J. Dölz, H. Harbrecht, S. Kurz, M. Multerer, S. Schöps, and F. Wolf. Bembel: The fast isogeometric boundary element C++ library for Laplace, Helmholtz, and electric wave equation. *SoftwareX* **11** (2020) 100476.
- [13] J. Dölz, H. Harbrecht, S. Kurz, M. Multerer, S. Schöps, and F. Wolf. Bembel: Boundary element method based engineering library. <http://www.bembel.eu>.
- [14] J. Dölz, H. Harbrecht, S. Kurz, S. Schöps, and F. Wolf. A fast isogeometric BEM for the three dimensional Laplace- and Helmholtz problems. *Comput. Methods Appl. Mech. Eng.* **330** (2018) 83–101.
- [15] J. Dölz, H. Harbrecht, and M. Peters. An interpolation-based fast multipole method for higher-order boundary elements on parametric surfaces. *Int. J. Numer. Meth. Eng.* **108** (2016) 1705–1728.
- [16] A. Ferrer, J.C. Cante, J.A. Hernández, and J. Oliver. Two-scale topology optimization in computational material design: An integrated approach. *Int. J. Numer. Meth. Eng.* **114** (2018) 232–254.
- [17] P. Geoffroy-Donders, G. Allaire, and O. Pantz. 3-d topology optimization of modulated and oriented periodic microstructures by the homogenization method. *J. Comput. Phys.* **401** (2020) 108994.
- [18] R. Ghanem and P. Spanos. *Stochastic finite elements: A spectral approach*. Springer, New York, 1991.
- [19] L. Greengard and V. Rokhlin. A fast algorithm for particle simulations. *J. Comput. Phys.* **73** (1987) 325–348.
- [20] L. Greengard and V. Rokhlin. On the numerical solution of two-point boundary value problems. *Commun. Pure Appl. Math.* **44** (1991) 419–452.
- [21] W. Hackbusch and S. Börm.  $\mathcal{H}^2$ -matrix approximation of integral operators by interpolation. *Appl. Numer. Math.* **43** (2002) 129–143.
- [22] J. Hadamard. *Lectures on the Calculus of Variations*. Gauthier-Villiers, Paris, 1910.
- [23] H. Harbrecht and M. Peters. Comparison of fast boundary element methods on parametric surfaces. *Comput. Methods Appl. Mech. Eng.* **261–262** (2013) 39–55.
- [24] H. Harbrecht, M. Peters, and R. Schneider. On the low-rank approximation by the pivoted Cholesky decomposition. *Appl. Numer. Math.* **62** (2012) 28–440.
- [25] H. Harbrecht, M. Peters, and M. Siebenmorgen. Efficient approximation of random fields for numerical applications. *Numer. Linear Algebra Appl.* **22** (2015) 596–617.
- [26] S.J. Hollister, R.D. Maddox, and J.M. Taboas. Optimal design and fabrication of scaffolds to mimic tissue properties and satisfy biological constraints. *Biomaterials* **23** (2002) 4095–4103.
- [27] N. Hopkinson, R. Hague, P. Dickens. *Rapid Manufacturing: An Industrial Revolution for the Digital Age*, John Wiley & Sons, 2006.
- [28] D. Hübner, E. Rohan, V. Lukeš, and M. Stingl. Optimization of the porous material described by the Biot model. *Int. J. Solids Struct.* **156–157** (2019) 216–233.

- [29] T.J.R. Hughes, J.A. Cottrell, and Y. Bazilevs. Isogeometric analysis: CAD, finite elements, NURBS, exact geometry and mesh refinement. *Comput. Methods Appl. Mech. Eng.* **194** (2005) 4135–4195.
- [30] R. Huiskes, H. Weinans, H.J. Grootenboer, M. Dalstra, B. Fudala, and T.J. Slooff. Adaptive bone-remodeling theory applied to prosthetic-design analysis. *J. Biomechanics* **20** (1987) 1135–1150.
- [31] C.Y. Lin, N. Kikuchia, and S.J. Hollister. A novel method for biomaterial scaffold internal architecture design to match bone elastic properties with desired porosity. *J. Biomechanics* **37** (2004) 623–636.
- [32] M. Loève. *Probability theory. I+II*. Graduate Texts in Mathematics, vol. 45, 4th edn. Springer, New York, 1977.
- [33] D. Luo, Q. Rong, and Q. Chen. Finite-element design and optimization of a three-dimensional tetrahedral porous titanium scaffold for the reconstruction of mandibular defects. *Med. Eng. Phys.* **47** (2017) 176–183.
- [34] F. Murat and J. Simon. Étude de problèmes d’optimal design. In *Optimization techniques, modeling and optimization in the service of man*, edited by J. Cea, Lect. Notes Comput. Sci. 41, Springer, Berlin, 54–62 (1976).
- [35] G. Nika and A. Constantinescu. Design of multi-layer materials using inverse homogenization and a level set method. *Comput. Methods Appl. Mech. Engrg.* **346** (2019) 388–409.
- [36] G. Nguetseng. A general convergence result related to the theory of homogenization. *SIAM J. Math. Anal.* **20** (1989) 608–629.
- [37] D.K. Pattanayak, A. Fukuda, T. Matsushita, M. Takemoto, S. Fujibayashi, K. Sasaki, N. Nishida, T. Nakamura, and T. Kokubo. Bioactive Ti metal analogous to human cancellous bone. Fabrication by selective laser melting and chemical treatments. *Acta Biomaterialia* **7** (2011) 1398–1406.
- [38] O. Pironneau. *Optimal Shape Design for Elliptic Systems*. Springer, New York, 1984.
- [39] G. Rotta, T. Seramak, and K. Zasińska. Estimation of Young’s modulus of the porous titanium alloy with the use of FEM package. *Adv. Mat. Sci.* **15** (2015) 29–37
- [40] F. Schury, M. Stingl, and F. Wein. Efficient two-scale optimization of manufacturable graded structures. *SIAM J. Sci. Comput.* **34** (2012) B711–B733.
- [41] O. Sigmund. Tailoring materials with prescribed elastic properties. *Mech. Mat.* **20** (1995) 351–368.
- [42] J. Simon. Differentiation with respect to the domain in boundary value problems. *Numer. Funct. Anal. Optim.* **2** (1980) 649–687.
- [43] J. Sokolowski and J.-P. Zolesio. *Introduction to Shape Optimization: Shape Sensitivity Analysis*. Springer, 1992.
- [44] L. Tartar. *The General Theory of Homogenization. A Personalized Introduction*. Lecture Notes of the Unione Matematica Italiana, vol. 7, Springer, 2010.
- [45] Y. Wang and Z. Kang. Concurrent two-scale topological design of multiple unit cells and structure using combined velocity field level set and density mode. *Comput. Methods Appl. Mech. Engrg.* **347** (2019) 340–364.
- [46] X. Wang, S. Xu, S. Zhou, W. Xu, M. Leary, P. Choong, M. Qian, M. Brandt, and Y.M. Xie. Topological design and additive manufacturing of porous metals for bone scaffolds and orthopaedic implants: A review. *Biomaterials* **83** (2016) 127–141.
- [47] M. Wormser, F. Wein, M. Stingl, and C. Körner. Design and additive manufacturing of 3D phononic band gap structures based on gradient based optimization. *Materials* **10** (2017) 1125.
- [48] L. Xia and P. Breitkopf. Multiscale structural topology optimization with an approximate constitutive model for local material microstructure. *Comput. Methods Appl. Mech. Engrg.* **286** (2015) 147–167.

HELMUT HARBRECHT AND REMO VON RICKENBACH, DEPARTEMENT FÜR MATHEMATIK UND INFORMATIK, UNIVERSITÄT BASEL, SPIEGELGASSE 1, 4051 BASEL, SWITZERLAND.

*Email address:* {`helmut.harbrecht,remo.vonrickenbach`}@unibas.ch

MICHAEL MULTERER, EULER INSTITUTE, USI LUGANO, VIA LA SANTA 1, 6900 LUGANO, SVIZZERA.

*Email address:* michael.multerer@usi.ch